USING 2D-FFT TO SEARCH FAST RADIO BURST[*]

C.H. Niu,[1,2,3] Y.C. Li,[2] F.Q. Wu,[2] Ue-li Pen,[4,2] and X.L. Chen[2]

[1] *Central China Normal University*

Luoyu Road,Wuhan, China
[2] *National Astronomy Observatory , Chinese Academy of Sciences*

Datun(A) Road,No.30,Beijing, China
[3] *University of California Berkeley, Campbell Hall 339, Berkeley CA 94720*
[4] *CITA*

ABSTRACT

Fast Radio Burst have been found from pulsar data for many years. There are several FRB search algorithm like tree algorithm ,FDMT et. Here we proposed a different FRB searching algorithm which basically trace a curve in frequency-time image. This algorithm is mainly realized by two dimensional Fast Fourier Transform. This will bring a speed up benefit in well-developed 2D FFT library both in CPU and GPU code. We take a 2D FFT on the $f^{-2}(t)$ data map, if there is a FRB signal , it will shows up in the center and perpendicular to the original one in map after 2D FFT.

Fast Radio Burst is a high energy radio signal found in the Universe. The first one is found by Lorimer Duncn in 2007, now people always call it as Lormeter burst. Like Pulsar, Its a wide band radio sginal, when it go through the inter stellar or inter galaxy medium, the higher frequency will go faster than lower frequency. When Signal go through dense of ISM The origin of FRB is still unclear, there are lots of theories trying to describe what FRB is.

The precise localization of the repeating fast radio burst (FRB Search Algorithm) has provided the first unambiguous association (chance coincidence probability $p \lesssim 3 \times 10^{-4}$) of an FRB with an optical and persistent radio counterpart. We report on optical imaging and spectroscopy of the counterpart and find that it is an extended ($0\rlap{.}''6 - 0\rlap{.}''8$) object displaying prominent Balmer and [O III] emission lines. Based on the spectrum and emission line ratios, we classify the counterpart as a low-metallicity, star-forming, $m_{r'} = 25.1$ AB mag dwarf galaxy at a redshift of $z = 0.19273(8)$, corresponding to a luminosity distance of 972 Mpc. From the angular size, the redshift, and luminosity, we estimate the host galaxy to have a diameter $\lesssim 4$ kpc and a stellar mass of $M_* \sim 4 - 7 \times 10^7 \, M_\odot$, assuming a mass-to-light ratio between 2 to $3 \, M_\odot \, L_\odot^{-1}$. Based on the H$\alpha$ flux, we estimate the star formation rate of the host to be $0.4 \, M_\odot \, \mathrm{yr}^{-1}$ and a substantial host dispersion measure depth $\lesssim 324$ pc cm^{-3}. The net dispersion measure contribution of the host galaxy to FRB Search Algorithm is likely to be lower than this value depending on geometrical factors. We show that the persistent radio source at FRB Search Algorithm's location reported by Marcote et al. (2017) is offset from the galaxy's center of light by $\sim$200 mas and the host galaxy does not show optical signatures for AGN activity. If FRB Search Algorithm is typical of the wider FRB population and if future interferometric localizations preferentially find them in dwarf galaxies with low metallicities and prominent emission lines, they would share such a preference with long gamma ray bursts and superluminous supernovae.

Keywords: stars: neutron – stars: magnetars – galaxies: distances and redshifts – galaxies: dwarf – galaxies: ISM

Corresponding author: Xuelei Chen

[*] peterniu@nao.cas.cn

1. INTRODUCTION

Fast radio bursts (FRBs) are bright ($\sim$Jy) and short ($\sim$ms) bursts of radio emission that have dispersion measures (DMs) in excess of the line of sight DM contribution expected from the electron distribution of our Galaxy. To date 18 FRBs have been reported — most of them detected at the Parkes telescope (Lorimer et al. 2007; Thornton et al. 2013; Burke-Spolaor & Bannister 2014; Keane et al. 2012; Ravi et al. 2015; Petroff et al. 2015; Keane et al. 2016; Champion et al. 2016; Ravi et al. 2016) and one each at the Arecibo (Spitler et al. 2014) and Green Bank telescopes (Masui et al. 2015).

A plethora of source models have been proposed to explain the properties of FRBs (see e.g. Katz 2016, for a brief review). According to the models, the excess DM for FRBs may be intrinsic to the source, placing it within the Galaxy; it may arise mostly from the intergalactic medium, placing a source of FRBs at cosmological distances ($z \sim 0.2 - 1$) or it may arise from the host galaxy, placing a source of FRBs at extragalactic, but not necessarily cosmological, distances ($\sim 100\,\mathrm{Mpc}$).

Since the only evidence to claim an extragalactic origin for FRBs has been the anomalously high DM, some models also attempted to explain the excess DM as a part of the model, thus allowing FRBs to be Galactic. All FRBs observed to date have been detected with single dish radio telescopes, for which the localization is of order arcminutes, insufficient to obtain an unambiguous association with any object. To date, no independent information about their redshift, environment, and source could be obtained due to the lack of an accurate localization of FRBs. Keane et al. (2016) attempted to identify the host of FRB 150418 on the basis of a fading radio source in the field that was localized to a $z = 0.492$ galaxy. However, later work identified the radio source as a variable active galactic nucleus (AGN) that may not be related to the source (Williams & Berger 2016; Bassa et al. 2016; Giroletti et al. 2016; Johnston et al. 2017).

Repeated radio bursts were observed from the location of the Arecibo-detected FRB Search Algorithm (Spitler et al. 2016; Scholz et al. 2016), with the same DM as the first detection, indicating a common source. As discussed by Spitler et al. (2016), it is unclear whether the repetition makes FRB Search Algorithm unique among known FRBs, or whether radio telescopes other than Arecibo lack the sensitivity to readily detect repeat bursts from other known FRBs.

Chatterjee et al. (2017) used the Karl G. Jansky Very Large Array (VLA) to directly localize the repeated bursts from FRB Search Algorithm with 100-mas precision and reported an unresolved, persistent radio source and an extended optical counterpart at the location with a chance coincidence probability of $\approx 3 \times 10^{-4}$ — the first unambiguous identification of multi-wavelength counterparts to FRBs. Independently, Marcote et al. (2017) used the European VLBI Network (EVN) to localize the bursts and the persistent source and showed that both are co-located within ~ 12 milliarcseconds.

Here we report the imaging and spectroscopic follow-up of the optical counterpart to FRB Search Algorithm using the 8-m Gemini North telescope.

2. OBSERVATIONS AND DATA ANALYSIS

The location of FRB Search Algorithm was observed with the Gemini Multi-Object Spectrograph (GMOS) instrument at the 8-m Gemini North telescope atop Mauna Kea, Hawai'i. Imaging observations were obtained with SDSS r', i' and z' filters on 2016 October 24, 25, and November 2, under photometric and clear conditions with $0\!''\!.58$ to $0\!''\!.66$ seeing. Exposure times of $250\,\mathrm{s}$ were used in the r' filter and of $300\,\mathrm{s}$ in the i' and z' filters with total exposures of $1250\,\mathrm{s}$ in r', $1000\,\mathrm{s}$ in i' and $1500\,\mathrm{s}$ in z'. The detectors were read out with 2×2 binning, providing a pixel scale of $0\!''\!.146\,\mathrm{pix}^{-1}$. The images were corrected for a bias offset, as measured from the overscan regions, flat fielded using sky flats and then registered and co-added.

The images were astrometrically calibrated against the *Gaia* DR1 Catalog (Gaia Collaboration et al. 2016). To limit the effects of distortion, the central $2\!'\!.2 \times 2\!'\!.2$ subsection of the images were used. Each of the r', i', and z' images were matched with $35 - 50$ unblended stars yielding an astrometric calibration with $7 - 9\,\mathrm{mas}$ root-mean-square (rms) position residuals in each coordinate after iteratively removing $\sim 4 - 5$ outliers. The error in the mean astrometric position with respect to the *Gaia* frame is thus $\sim 1 - 2\,\mathrm{mas}$.

We used the `Source Extractor` (Bertin & Arnouts 1996) software to detect and extract sources in the coadded images. The r' and i' images were photometrically calibrated with respect to the IPHAS DR2 catalog (Barentsen et al. 2014) using Vega-AB magnitude conversions stated therein. We measure isophotal integrated magnitudes of $m_{r'} = 25.1 \pm 0.1\,\mathrm{AB}$ mag and $m_{i'} = 23.9 \pm 0.1\,\mathrm{AB}$ mag for the optical counterpart of FRB Search Algorithm. The error value includes the photometric errors and rms zero-point scatter. Ongoing observations will provide full photometric calibration in g', r', i', and z' bands and will be reported in a subsequent publication.

Spectroscopic observations were obtained with GMOS on 2016 November 9 and 10 with the $400\,\mathrm{lines\,mm}^{-1}$ grating (R400) in combination with a $1''$ slit, covering
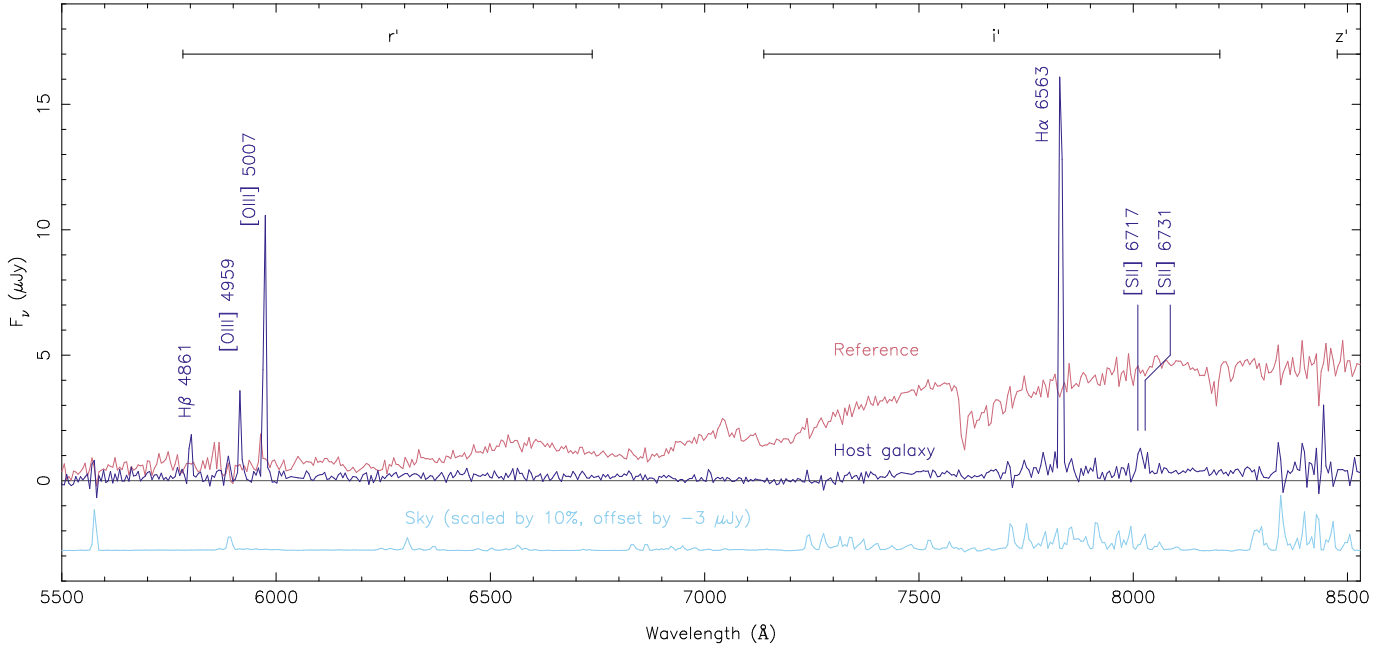
Figure 1. The co-added spectrum of the host galaxy of FRB Search Algorithm, the reference object, and the sky contribution (scaled by 10% and offset by $-3\,\mu$Jy). The spectra have been resampled to the instrumental resolution. Prominent emission lines are labelled with their rest frame wavelengths. Black horizontal bars denote the wavelength ranges of the filters used for imaging. Most of the wavelength coverage of the z' band is outside the coverage of this plot.

the wavelength range from 4650 to 8900 Å. A total of nine 1800 s exposures were taken with 2×2 binning, providing a spatial scale of $0\rlap{.}''292\,\mathrm{pix}^{-1}$ and an instrumental resolution of 4.66 Å, sampled at $1.36\,\mathrm{\AA\,pix}^{-1}$. The conditions were clear, with $0\rlap{.}''8$ to $1\rlap{.}''0$ seeing on the first night, and $0\rlap{.}''9$ to $1\rlap{.}''1$ on the second. To aid the spectral extraction of the very faint counterpart, the slit was oriented at a position angle of $18\rlap{.}°6$, containing the counterpart to FRB Search Algorithm as well as an $m_{r'} = 24.3$ AB mag, $m_{i'} = 22.7$ AB mag foreground star, located $2\rlap{.}''8$ to the South (shown later in Figure **??**).

The low signal-to-noise of the spectral trace of the FRB counterpart on the individual bias-corrected long-slit spectra complicated spectral extraction through the optimal method by Horne (1986). Instead, we used a variant of the optimal extraction method of Hynes (2002) by modelling the spectral trace of the reference object by a Moffat function (Moffat 1969) to determine the position and width of the spatial profile as a function of wavelength. Because of the proximity of the reference object to the FRB counterpart (20 pix), we assume that the spatial profile as a function of wavelength is identical for both. We note that though the counterpart is slightly resolved in the imaging observations, the worse seeing during the spectroscopic observations (by a factor 1.2 to 1.9) means the seeing dominates the spatial profile. The residual images validate this assumption; no residual flux is seen once the extracted model is sub-

tracted from the image. To optimally extract the spectra of the FRB counterpart, the reference object as well as the sky background, we then simultaneously fit the spatial profile at the location of the counterpart and at the location of the reference object on top of a spatially varying linear polynomial for each column in the dispersion direction.

Wavelength calibrations were obtained from arc lamp exposures, modelling the dispersion location to wavelength through 4th order polynomials, yielding rms residuals of better than 0.2 Å. The individual wavelength calibrated spectra were then combined and averaged. The instrumental response of the spectrograph was calibrated using an observation of the spectrophotometric standard Hiltner 600 (Hamuy et al. 1992, 1994), which was taken on 2016 November 7 as part of the standard Gemini calibration plan with identical instrumental setup as the science observations. The flux-calibrated spectrum of the reference object gives a spectroscopic AB magnitude of $m_{i'} \approx 22.6$, about 11% higher than derived from photometry. Given that the spectrophotometric standard was observed on a different night with worse seeing $(1\rlap{.}''4)$, we attribute this difference to slit losses and scale the flux of the observed spectra of the reference object and the FRB counterpart by a factor 0.89.

3. RESULTS AND ANALYSIS

The final combined and calibrated spectrum is shown in Figure **??**. Besides continuum emission, which is weakly detected in the red part of the spectrum, four strong emission lines are clearly visible and are identified as Hα, Hβ, and [O III] $\lambda4959$ and [O III] $\lambda5007$ indicating that the optical counterpart is a star-forming galaxy. The corresponding weighted mean redshift is $z = 0.19273 \pm 0.0008$. Weaker emission lines from [S II] $\lambda\lambda6717, 6731$ are also detected. The [N II] $\lambda\lambda6549, 6583$ and the [O I] $\lambda6300$ lines are not seen.

Gaussian fits to the emission lines in the rest frame yield the flux and 1-σ width values listed in Table **??**. We estimate rest frame equivalent widths for the strongest emission lines; 392 ± 102 Å for [O III] $\lambda5007$ and 290 ± 55 Å for Hα.

The ratios of measured line fluxes for [O III]/Hβ against [N II]/Hα and [S II]/Hα— the well-known Baldwin, Phillips & Terlevich (BPT) diagram (Baldwin et al. 1981) — are shown in Figure **??**. The line ratios of the host galaxy of FRB Search Algorithm are compared to those from the SDSS DR12 galaxy sample (Alam et al. 2015). The locations below and to the left of the solid and dashed grey lines indicate that the emission lines are due to star formation and not due to AGN activity (Kewley et al. 2001, 2006; Kauffmann et al. 2003). Note that the BPT diagram line ratios are insensitive to reddening (from the Milky Way as well as the host itself).

We use the `galfit` software (Peng et al. 2002, 2010) to constrain the morphology of the optical counterpart. A Sérsic profile ($\Sigma(r) = \Sigma_{\mathrm{e}}e^{-\kappa[(r/R_{\mathrm{e}})^{1/n}-1]}$), convolved with the point-spread-function, was fitted against the spatial profile of the counterpart. For the i'-band image, the best fit has an effective radius of $R_{\mathrm{e}} = 0\rlap{.}''41 \pm 0\rlap{.}''06$, a Sérsic index of $n = 2.2 \pm 1.5$, and an ellipticity of $b/a = 0.25 \pm 0.13$. The lower signal-to-noise of the counterpart in the r' and z' images did not permit meaningful results. Instead, we directly fit the spatial profile in all three bands with a two-dimensional elliptical Gaussian profile. In the case of the i'-band image, the fit provides a position and effective radius, taken as the Gaussian σ, consistent with the Sérsic profile convolved with the point-spread-function. The results of the fits are shown in Figure **??**.

The position and extent of the host galaxy, as approximated with the two-dimensional elliptical Gaussian profile, agrees well in the r' and i' bands (semi-major axis $\sigma_a = 0\rlap{.}''44$ with ellipticity $b/a = 0.68$), while the z'-band has a slightly offset position and appears larger ($\sigma = 0\rlap{.}''59$ with $b/a = 0.45$). We attribute this difference to the fact that the the r' and i' bands are dominated by the bright emission lines of Hα, Hβ, [O III] $\lambda4959$
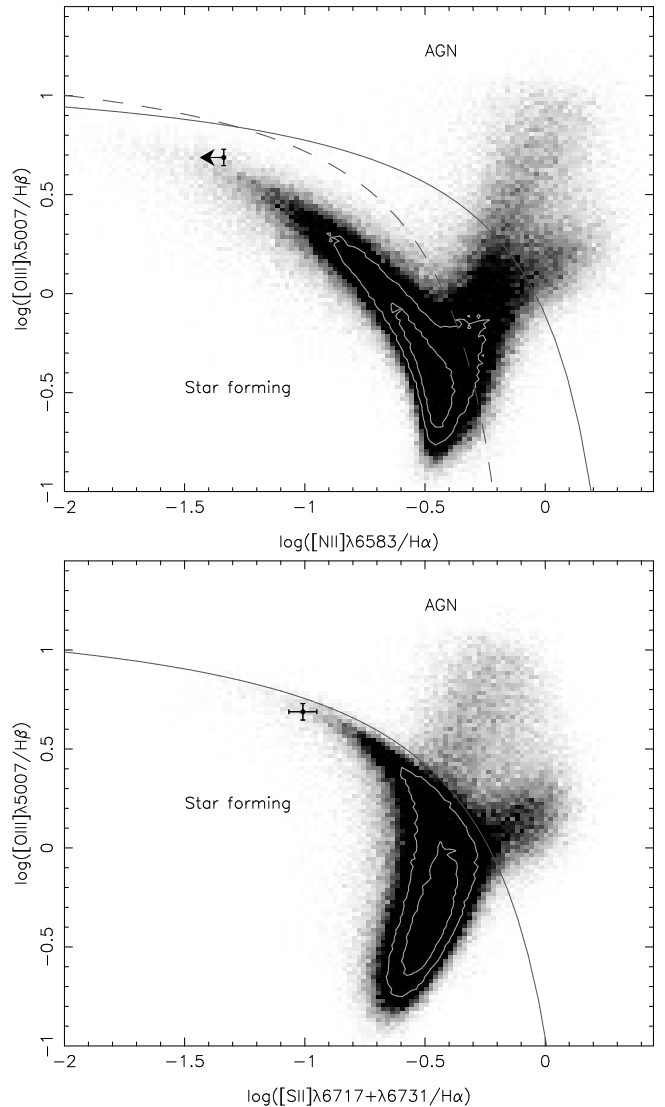

Figure 2. BPT (Baldwin et al. 1981) diagrams of [N II]/Hα and [S II]/Hα against [O III]/Hβ for the SDSS DR12 (Alam et al. 2015) galaxy sample with significant (>5-σ) emission lines. The black symbol with error bars denotes the location of the host galaxy of FRB 121102. The solid and dashed lines denote the demarcations between star-forming and AGN dominated galaxies, respectively (Kewley et al. 2001, 2006; Kauffmann et al. 2003). The region between the two curves corresponds to composite objects with AGN and star formation.

and [O III] $\lambda5007$, while the redder z'-band traces the continuum flux of the host galaxy. As such, the morphology suggests that the host galaxy has at least one H II region at a slight offset from the galaxy center.

Finally, the bottom right panel of Figure **??** plots the Gaussian centroids on the International Celestial Reference Frame (ICRF) through the astrometric calibration of the r', i', and z' images against *Gaia*. The positional uncertainties in each axis are the quadratic sum

Table 1. Emission line properties.

Line	Obs. Flux	Width (σ)	A_λ/A_V
	(erg cm^{-2} s^{-1})	(Å)	(mag)
Hβ	$0.118(11) \times 10^{-16}$	1.91(19)	0.941
[O III] λ4959	$0.171(10) \times 10^{-16}$	1.75(11)	0.921
[O III] λ5007	$0.575(11) \times 10^{-16}$	1.89(4)	0.911
[O I] λ6300	$< 0.009 \times 10^{-16}$		0.670
[N II] λ6549	$< 0.021 \times 10^{-16}$		0.625
Hα	$0.652(9) \times 10^{-16}$	2.02(3)	0.622
[N II] λ6583	$< 0.030 \times 10^{-16}$		0.619
[S II] λ6717	$0.040(6) \times 10^{-16}$	2.4(4)	0.596
[S II] λ6731	$0.024(6) \times 10^{-16}$	2.4(6)	0.593

NOTE—Observed emission line properties from fitting normalized Gaussians to the rest-wavelength host galaxy spectrum. Upper limits (3-σ) on line fluxes assume Gaussian widths of $\sigma = 2$ Å. The absorption A_λ/A_V at the observed line wavelengths is taken from Cardelli et al. (1989). To obtain unabsorbed line fluxes, multiply by $10^{0.4(A_\lambda/A_V)A_V}$, where A_V is the Galactic absorption towards FRB 121102.

of the astrometric tie against *Gaia* (of order 2 mas) and the centroid uncertainty on the image (between 20 and 50 mas). The *Gaia* frame is tied to the ICRF defined via radio VLBI to a $\sim$1 mas precision (Mignard et al. 2016), much smaller than the centroid uncertainty. We find that the position of the persistent radio source seen with the EVN at an observing frequency of 5 GHz with a 1-mas precision (Marcote et al. 2017), is offset from the galaxy centroids by 186 ± 68 and 163 ± 32 mas in the line-dominated r' and i' images, and 286 ± 64 mas in the continuum-dominated z' image. Though offset from the centroids, the persistent radio source is located within the effective radii of the different bands.

4. DISCUSSION AND CONCLUSIONS

The observations presented here confirm the interpretation by Chatterjee et al. (2017) that the extended optical counterpart associated with FRB Search Algorithm is the host galaxy of the FRB. Our measurement of the redshift $z = 0.19273$ is consistent with the DM-estimated value of $z_{DM} < 0.32$ (Chatterjee et al. 2017) and together with the very low chance superposition probability, firmly places FRB Search Algorithm at a cosmological distance, ruling out all Galactic models for this source.

In the following discussion, we assume the cosmological parameters from the Planck Collaboration et al. (2016) as implemented in `astropy.cosmology` (Astropy
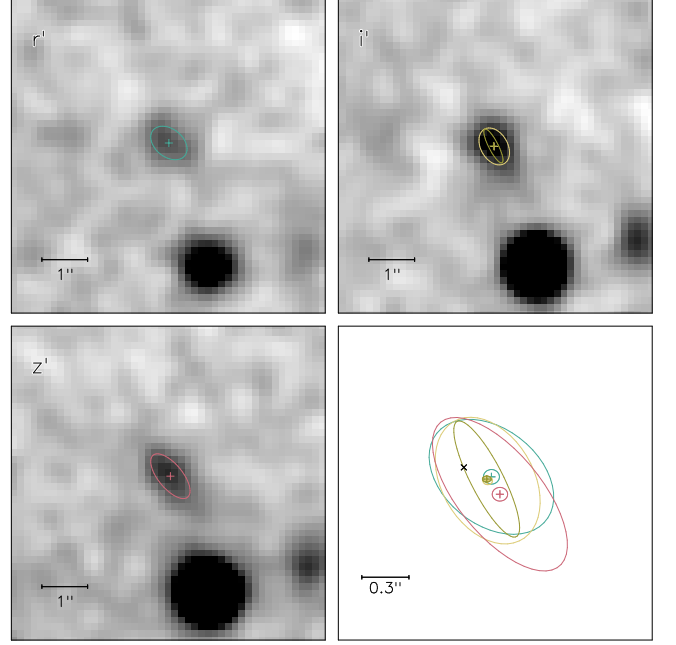

Figure 3. The top left, top right and bottom left panels show respective $7\rlap{.}''4 \times 7\rlap{.}''4$ subsections of the GMOS r', i' and z' images, centered on the optical counterpart to FRB 121102. Each image has been smoothed by a Gaussian with a width of $0\rlap{.}''2$, while the plus sign and ellipse denote the position and extent of a two-dimensional Gaussian fit to the spatial profile of the counterpart. The i'-band image also shows the narrower Sérsic fit by `galfit`. The bottom right panel combines the positional and morphological measurements from the different bands on an astrometric frame of $1'' \times 1''$ in size. The colors are identical to those used in the other panels. The large ellipses denote the extent of the Gaussian and Sérsic fits, while the small ellipses denote the 1-σ absolute positional uncertainties. The location of the persistent counterpart as measured with the EVN at 5 GHz by Marcote et al. (2017) is represented by the black cross. The uncertainty in the EVN location is much smaller than the size of the symbol.)

Collaboration et al. 2013), giving a luminosity distance of $D_L = 972$ Mpc, and $1''$ corresponding to projected proper and comoving distances of 3.31 kpc and 3.94 kpc, respectively.

We use the Schlegel et al. (1998) estimate of the Galactic extinction along this line of sight[1], $E_{B-V} = 0.781$. Using $R_V = 3.1$, we find $A_V = 2.42$, and use the Cardelli et al. (1989) Galactic extinction curve to correct the spectrum with band extinctions of $A_{r'} = 2.15$, $A_{i'} = 1.63$, and $A_{z'} = 1.16$ mag. We note that the Schlafly et al. (2010); Schlafly & Finkbeiner (2011) recalibrated extinction model predicts a slightly lower extinction of

---

[1] From the IRSA Dust Extinction Calculator http://irsa.ipac.caltech.edu/applications/DUST/

$E_{B-V} = 0.673$. The results described below are insensitive to differences in the extinction at this level. We do not apply k-correction to the magnitudes as they are not needed for the precision discussed here.

4.1. Burst Energetics

The redshift measurement allows us to put FRB Search Algorithm's energetics on a firmer footing, confirming the energy scale of $10^{38}\,\mathrm{erg}\,(\delta\Omega/4\pi)(A_\nu/0.1\,\mathrm{Jy\,ms})(\Delta\nu/1\,\mathrm{GHz})$ calculated by Chatterjee et al. (2017) using a distance scale of $1\,\mathrm{Gpc}$. Here A_ν and $\Delta\nu$ are the fluence and bandwidth, respectively, at observing frequency ν and $\delta\Omega$ is the opening angle of the bursts. A more detailed analysis of energetics of individual bursts detected by the VLA and their rates will be reported in Law C. J. et al. (in preparation).

4.2. Physical Properties of the Host

The host of FRB Search Algorithm is a small galaxy with a diameter of $\lesssim 4\,\mathrm{kpc}$, inferred from the continuum-dominated z'-band image. The absolute magnitudes, including the emission line fluxes and after correcting for the Milky Way's extinction, are $M_{r'} = -17.0\,\mathrm{AB}$ mag and $M_{i'} = -17.7\,\mathrm{AB}$ mag, identifying the host as a dwarf galaxy.

From Table **??**, the Hα luminosity of the host galaxy, corrected for Milky Way extinction, is $L_{\mathrm{H}\alpha} = 2.9 \times 10^{40}\,\mathrm{erg\,s^{-1}}$. The corresponding star formation rate is $\mathrm{SFR(H}\alpha) = 7.9 \times 10^{-42}\,M_\odot\,\mathrm{yr^{-1}} \times (L_{\mathrm{H}\alpha}/\mathrm{erg\,s^{-1}}) = 0.23\,M_\odot\,\mathrm{yr^{-1}}$ (Kennicutt et al. 1994). This value does not completely account for the extinction of Hα photons in the host galaxy. The correction suggested by Kewley et al. (2002) is $\mathrm{SFR}(IR) = 2.7 \times \mathrm{SFR(H}\alpha)^{1.3} \approx 0.4\,M_\odot\,\mathrm{yr^{-1}}$ (in the 8–1000 μm band). This is consistent with the 3-σ upper limit of $< 9\,M_\odot\,\mathrm{yr^{-1}}$ estimated from the ALMA non-detection of the host at $230\,\mathrm{GHz}$ assuming a submillimeter spectral index $\alpha = 3$ (Chatterjee et al. 2017).

The mass-to-light ratio Υ_* is dependent on the star formation history and the initial mass function for star formation. As an estimate, we use $\Upsilon_*^R \approx 2 - 3\,M_\odot\,L_\odot^{-1}$ based on the dynamics of dwarf galaxies with high star formation rates (Lelli et al. 2014), implying a stellar mass $M_* \sim 4 - 7 \times 10^7\,M_\odot$. As dwarf galaxies are usually gas-rich (e.g. Papastergis et al. 2012), we expect that this estimate is a lower limit to the host baryonic mass. We also note that dwarf galaxies are typically dark matter dominated (Côté et al. 2000), and so the total dynamical mass is likely to be larger.

We use the R_{23} (Kewley & Dopita 2002), $N2$, $O3N2$ (Pettini & Pagel 2004), and the recently defined diagnostic of Dopita et al. (2016, labelled here as y) to estimate the metallicity where,

$$R_{23} = \log_{10}((\mathrm{[O\,II]}\lambda3727 + \mathrm{[O\,III]}\lambda\lambda4959, 5007)/\mathrm{H}\beta),$$
$$N2 = \log_{10}(\mathrm{[N\,II]}\lambda6584/\mathrm{H}\alpha),$$
$$O3N2 = \log_{10}(\mathrm{[O\,III]}\lambda5007)/\mathrm{[N\,II]}\lambda6584 \times \mathrm{H}\alpha/\mathrm{H}\beta),\ \mathrm{and}$$
$$y = \log_{10}(\mathrm{[N\,II]}\lambda6584/\mathrm{[S\,II]}\lambda\lambda6717, 6731)$$
$$+ 0.264\log_{10}(\mathrm{[N\,II]}\lambda6584/\mathrm{H}\alpha).$$

As the [O II]$\lambda3727$ line is outside our spectral coverage and [N II]$\lambda6584$ is not detected, we can only set an upper limit to the metallicity. Using the extinction-corrected line fluxes, we measure,

$$R_{23} \geq 0.77,$$
$$N2 \leq -1.34,$$
$$O3N2 \geq 2.1,$$
$$y \leq -0.66,$$

where the limits are calculated from the 3-σ limit on [N II]$\lambda6584$ flux and assuming the lower limit for the unmeasured [O II]$\lambda3727$ flux to be zero. This corresponds to a 3-σ metallicity limit of $\log_{10}(\mathrm{[O/H]}) + 12 < 8.4$ (Kewley & Dopita 2002), < 8.4 (Pettini & Pagel 2004, , $N2$), < 8.4 (Pettini & Pagel 2004, $O3N2$)[2] and < 8.1 (Dopita et al. 2016, not including scatter). We convert these into the oft-used KK04 scale (Kobulnicky & Kewley 2004) using the conversions of Kewley & Ellison (2008). All measurements are consistent with $\log_{10}(\mathrm{[O/H]}) + 12 \lesssim 8.7$ in the KK04 scale. The metallicity of the host is low — less than $\sim$15% of all galaxies brighter than $M_B < -16$ have metallicity lower than 8.7 (Graham & Fruchter 2015). This set of galaxies account for less than 20% of the star formation of the local Universe.

The host properties are similar to those of extreme emission line galaxies (EELGs; Atek et al. 2011), young, low-mass starbursts which have emission lines of rest-frame equivalent widths greater than 200Å.

4.3. Ionized Gas Properties in the Host

The Balmer lines from the host also allow us to estimate the properties its ionized ISM and its contribution to the total DM of FRB Search Algorithm.

The Hα surface density for the galaxy with flux $F_{\mathrm{H}\alpha}$, semi-major axis a, and semi-minor axis b is

$$S(\mathrm{H}\alpha) = \frac{F_{\mathrm{H}\alpha}}{\pi ab},$$

---

[2] We note that the Pettini & Pagel (2004) calibration has high scatter for $O3N2 \gtrsim 2$ but the limit quoted here includes the scatter.

$$\approx 6.8 \times 10^{-16} \, \text{erg cm}^{-2} \, \text{s}^{-1} \, \text{arcsecond}^{-2},$$
$$\approx 120 \, \text{Rayleigh}, \qquad (1)$$

where we have used the extinction corrected flux $F_{\text{H}\alpha} = 2.6 \times 10^{-16} \, \text{erg cm}^{-2} \, \text{s}^{-1}$ and the semi-major and minor axes ($a = 0\rlap{.}''44$, $b/a = 0.68$) from the i' and r' images. In the source frame (denoted below by the subscript, 's'), the surface density is

$$S(\text{H}\alpha)_{\text{s}} = (1+z)^4 S(\text{H}\alpha) = 243 \, \text{Rayleigh}. \qquad (2)$$

For a temperature $T = 10^4 T_4$ K, we express the emission measure (EM $= \int n_e^2 \mathrm{d}s$) given by Reynolds (1977) in the galaxy's frame

$$\text{EM}(\text{H}\alpha)_{\text{s}} = 2.75 \text{pc cm}^{-6} \, T_4^{0.9} \left[\frac{S(\text{H}\alpha)_{\text{s}}}{\text{Rayleigh}} \right],$$
$$\approx 670 \, \text{pc cm}^{-6} \, T_4^{0.9}. \qquad (3)$$

We get a smaller value from the extinction-corrected Hβ flux, $\text{EM}(\text{H}\beta)_{\text{s}} \approx 530 \, \text{pc cm}^{-6}$. For the calculations below, we proceed with a combined estimate, $\text{EM}_{\text{s}} \approx 600 \, \text{pc cm}^{-6}$.

This value is fairly large compared to measurements of the local Galactic disk. The WHAM Hα survey, for example, gives values of tens of pc cm^{-6} in the Galactic plane and about 1 pc cm^{-6} looking out of the plane (Hill et al. 2008). However, lines of sight to distant pulsars and studies of other galaxies give EM values in the hundreds (Reynolds 1977; Haffner et al. 2009).

The estimate for EM$_{\text{s}}$ is sensitive to the inferred solid angle of the galaxy and emitting regions. Ongoing observations with the *Hubble Space Telescope* will better resolve the Hα emitting structures and improve our constraint on the EM with respect to the location of the burst.

The implied optical depth for free-free absorption at an observation frequency ν (in GHz) is

$$\tau_{\text{ff}} \approx 3.3 \times 10^{-6} [(1+z)\nu_{\text{GHz}}]^{-2.1} T_4^{-1.35} \text{EM}_{\text{s}}$$
$$\approx 1.4 \times 10^{-3} \nu_{\text{GHz}}^{-2.1} T_4^{-0.45}. \qquad (4)$$

Free-free absorption for FRB Search Algorithm is therefore negligible even at 100 MHz. This suggests that the radio spectra of the bursts and possibly the persistent source are unaffected by absorption and are inherent to the emission process or to propagation effects near the sources, confirming the inference made by (Scholz et al. 2016) based on the widely varying spectral shapes of the bursts alone.

4.3.1. *Implied DM from Hα-emitting Gas*

The EM implies a DM value sometimes given by $\text{DM} = (\text{EM} f_{\text{f}} L)^{1/2}$, where f_{f} is the volume filling factor of ionized clouds in a region of total size L (Reynolds 1977). As summarized in Appendix B of Cordes et al. (2016), additional fluctuations decrease the DM derived from EM, giving a source-frame value,

$$\widehat{\text{DM}}_{\text{s}} \approx 387 \, \text{pc cm}^{-3} \, L_{\text{kpc}}^{1/2} \left[\frac{f_{\text{f}}}{\zeta(1+\epsilon^2)/4} \right]^{1/2}$$
$$\times \left(\frac{\text{EM}}{600 \, \text{pc cm}^{-6}} \right)^{1/2}, \qquad (5)$$

where $\epsilon \leq 1$ is the fractional variation inside discrete clouds due to turbulent-like density variations and $\zeta \geq 1$ defines cloud-to-cloud density variations in the ionized region of depth L_{kpc} in kpc. Here we have used $\text{EM}_{\text{s}} = 600 \, \text{pc cm}^{-6}$ and assumed 100% cloud-to-cloud variations ($\zeta = 2$) and fully modulated electron densities inside clouds ($\epsilon = 1$).

The host contribution to the *measured* DM is a factor $(1+z)^{-1}$ smaller than the source frame DM[3]. Also, the line of sight to the FRB source may sample only a fraction of $\widehat{\text{DM}}_{\text{s}}$ depending on if it is embedded in or offset from the Hα-emitting gas. For an effective path length through the ionized gas $L_{\text{FRB}} \leq L$, we then have

$$\widehat{\text{DM}}(\text{FRB}) = \frac{\widehat{\text{DM}}_{\text{s}}}{1+z} \left(\frac{L_{\text{FRB}}}{L} \right)$$
$$\approx 324 \, \text{pc cm}^{-3} \left(\frac{L_{\text{FRB}}}{L} \right) \left[\frac{4 L_{\text{kpc}} f_{\text{f}}}{\zeta(1+\epsilon^2)} \right]^{1/2}. \qquad (6)$$

This estimate can be compared with empirical constraints discussed in Chatterjee et al. (2017) on contributions from the host and the intergalactic medium (IGM) to the total DM made by subtracting the NE2001 model's DM contribution from the Milky Way (Cordes & Lazio 2002) ($\text{DM}_{\text{MW}} = 188 \, \text{pc cm}^{-3}$) and the Milky Way halo ($\text{DM}_{\text{MW}_{\text{halo}}} = 30 \, \text{pc cm}^{-3}$) from the total DM $= 558 \, \text{pc cm}^{-3}$. This gives $\text{DM}_{\text{IGM}} + \text{DM}_{\text{host}} = 340 \, \text{pc cm}^{-3}$. The Milky Way contributions have uncertain errors but are likely of order 20%. The measured redshift implies a mean IGM contribution $\text{DM}_{\text{IGM}} \approx 200 \, \text{pc cm}^{-3}$ (Ioka 2003; Inoue 2004) but can vary by about $\pm 85 \, \text{pc cm}^{-3}$ (McQuinn 2014). This yields a range of possible values for DM_{host}: $55 \lesssim \text{DM}_{\text{host}} \lesssim 225 \, \text{pc cm}^{-3}$ that further implies $0.09 \lesssim (L_{\text{FRB}}/L) \left[L_{\text{kpc}} f_{\text{f}}/\zeta(1+\epsilon^2) \right]^{1/2} \lesssim 0.35$. The ionized region therefore must have some degree of clumpiness or the effective path length is significantly smaller than the size of the ionized region.

---

[3] The factor of $(1+z)^{-1}$ is a combination of the photon redshift, time dilation and the frequency^{-2} dependence of cold plasma dispersion.

Radio pulsars in the Large and Small Magellanic Clouds have DMs spanning the range 45–273 pc cm^{-3} and 70–200 pc cm^{-3}, respectively (Manchester et al. 2005). This empirically demonstrates that the free electron content of star-forming dwarf galaxies is of the order we estimate. The relatively large DM contribution from the host galaxy (as inferred from the Hα emission) implies that any contributions from the vicinity of the FRB source itself are probably quite small. This may rule out a very young (< 100 yr) supernova remnant (e.g. Piro 2016).

4.4. *Implications for Source Models*

Chatterjee et al. (2017) reported the locations of the radio bursts, the optical and variable radio counterparts and the absence of millimeter-wave and X-ray emission. Marcote et al. (2017) have shown that the bursts and the persistent radio source are colocated to within a linear projected separation of 40 pc, suggesting that the two emission sources should be physically related, though not necessarily the same source. The radio source properties are consistent with a low luminosity AGN or a young (<1000 yr) supernova remnant (SNR) powered by an energetic neutron star (e.g. Murase et al. 2016).

The optical properties of the galaxies reported here do not add support to the AGN interpretation although it cannot be conclusively ruled out. The BPT diagnostics for the host (Figure ??) show no indication of AGN activity. However, this may not be conclusive as the majority of radio-loud AGN show no optical signatures of activity (Mauch & Sadler 2007). This is further supported by five low luminosity AGN with no optical signatures have also recently been discovered (Park et al. 2016). However, these objects are almost exclusively hosted in galaxies with much larger stellar masses ($\sim 10^{10} M_\odot$). We also note that the radio source is offset from the optical center of the galaxy by 170–300 mas, corresponding to a transverse linear distance of 0.5–1 kpc, nearly a quarter to half of the radial extent, which is not consistent with a central AGN, but such offsets have been seen before in dwarf galaxies, e.g. Henize 2-10 (Reines et al. 2011).

The association of an optical/X-ray AGN with a dwarf galaxy is also extremely rare. A search of emission-line dwarf galaxies ($10^{8.5} \lesssim M_* \lesssim 10^{9.5} M_\odot$) using BPT line diagnostics identified an AGN rate of ~ 0.5 % (Reines et al. 2013), with an additional 0.05 % of dwarf galaxies searched exhibiting narrow emission lines consistent with star formation band broad Hα consistent with an AGN. Similarly, an X-ray survey of $z < 1$ dwarf galaxies reported an AGN rate of 0.6–3% (Pardo et al. 2016). Of the dwarf galaxies known to host AGN, only two exhibit

nuclear radio emission that appears to originate from a black-hole jet, Henize 2-10 and Mrk 709 (Reines et al. 2011, 2014). Both have strong nuclear X-ray emission that originates from the AGN but optical emission lines that are dominated by star-formation processes. The combination of a compact radio source, absent nuclear X-ray emission, strong star-formation optical emission lines, and weak or non-existent broad optical emission lines that we observe in the host of FRB Search Algorithm has no analogue in any known galaxy to the best of our knowledge.

The high star formation rate is consistent with the presence of a young SNR or a cluster of young massive stars (i.e. an OB association), which would naturally link FRBs to neutron stars which are the favored progenitor models.

4.4.1. *Relation to Dwarf Galaxies*

It is interesting to note that the only FRB host directly identified so far is a low metallicity dwarf galaxy rather than, say, an extremely high-star-formation-rate galaxy such as Arp 220 or a galaxy with a very powerful AGN or some other extreme characteristics. Dwarf galaxies are also a small fraction of the stellar mass in the Universe (Papastergis et al. 2012). Ravi et al. (2016) also suggested that the extremely low scattering of FRB 150807 compared to its DM may be linked to its origin from a low-mass ($< 10^9 M_\odot$) galaxy. However, the strong polarization and scattering properties of FRB 110523 do suggest the presence of turbulent magnetized plasma around the source (Masui et al. 2015), suggesting that individual FRB environments may be quite diverse.

If FRBs are indeed more commonly hosted by dwarf galaxies in the low redshift Universe, they would share this preference with two other classes of high-energy transients — long duration gamma-ray bursts and superluminous supernovae, both of which prefer low-mass, low-metallicity, and high star formation rate hosts (e.g., Fruchter et al. 2006; Perley et al. 2013; Vergani et al. 2015; Perley et al. 2016, and other works). Indeed, superluminous supernovae are prefentially hosted by EELGs (Leloudas et al. 2015). If this relation is true, it may point to a link between FRBs and extremely massive progenitor stars, possibly extending to magnetars that have been associated with massive progenitor stars (e.g. Olausen & Kaspi 2014).

4.5. *Future Optical Follow-Up of FRBs*

A link between FRBs and dwarf galaxies will impact future multi-wavelength follow-up plans. Without the precise localization for FRB Search Algorithm (Chatter-

jee et al. 2017), the host galaxy is scarcely distinguishable from other objects in the deep Gemini images.

Due to the trade-off between field of view and localization precision, FRB search projects that have a large FRB detection rate such as CHIME (Kaspi V. M. et al,. 2017, in preparation), UTMOST (Caleb et al. 2016), and HIRAX (Newburgh et al. 2016) will localize high signal to noise detections to only sub-arcmin precision. If FRB hosts are star-forming galaxies with strong emission lines, slitless objective prism spectroscopy could efficiently distinguish these objects from a field of stars and elliptical galaxies, leading to putative host identifications without very precise localization. However, this strongly depends on the link between FRBs and their host properties and the homogeneity of FRBs — which will first have to be confirmed with more interferometric localizations.

We note, of course, that our above discussion regarding the possible relationship between FRBs and dwarf galaxies in general is based on a single data point of a repeating FRB, which may not be representative of the broader FRB population (see Spitler et al. 2016; Scholz et al. 2016, for more details).

Facility: Gemini:Gillett (GMOS)

Software: ESO-MIDAS, astro-py, galfit, SExtractor

REFERENCES

Alam, S., Albareti, F. D., Allende Prieto, C., et al. 2015, ApJS, 219, 12

Astropy Collaboration, Robitaille, T. P., Tollerud, E. J., et al. 2013, A&A, 558, A33

Atek, H., Siana, B., Scarlata, C., et al. 2011, ApJ, 743, 121

Baldwin, J. A., Phillips, M. M., & Terlevich, R. 1981, PASP, 93, 5

Barentsen, G., Farnhill, H. J., Drew, J. E., et al. 2014, MNRAS, 444, 3230

Bassa, C. G., Beswick, R., Tingay, S. J., et al. 2016, MNRAS, 463, L36

Bertin, E., & Arnouts, S. 1996, A&AS, 117, 393

Burke-Spolaor, S., & Bannister, K. W. 2014, ApJ, 792, 19

Caleb, M., Flynn, C., Bailes, M., et al. 2016, MNRAS, 458, 718

Cardelli, J. A., Clayton, G. C., & Mathis, J. S. 1989, ApJ, 345, 245

Champion, D. J., Petroff, E., Kramer, M., et al. 2016, MNRAS, 460, L30

Chatterjee, S., Law, C. J., Wharton, R. S., et al. 2017, Nature, 000, 000

Cordes, J. M., & Lazio, T. J. W. 2002, ArXiv Astrophysics e-prints, astro-ph/0207156

Cordes, J. M., Wharton, R. S., Spitler, L. G., Chatterjee, S., & Wasserman, I. 2016, ArXiv e-prints, arXiv:1605.05890

Côté, S., Carignan, C., & Freeman, K. C. 2000, AJ, 120, 3027

Dopita, M. A., Kewley, L. J., Sutherland, R. S., & Nicholls, D. C. 2016, Ap&SS, 361, 61

Fruchter, A. S., Levan, A. J., Strolger, L., et al. 2006, Nature, 441, 463

Gaia Collaboration, Brown, A. G. A., Vallenari, A., et al. 2016, ArXiv e-prints

Giroletti, M., Marcote, B., Garrett, M. A., et al. 2016, A&A, 593, L16

Graham, J. F., & Fruchter, A. S. 2015, ArXiv e-prints, arXiv:1511.01079

Haffner, L. M., Dettmar, R.-J., Beckman, J. E., et al. 2009, Reviews of Modern Physics, 81, 969

Hamuy, M., Suntzeff, N. B., Heathcote, S. R., et al. 1994, PASP, 106, 566

Hamuy, M., Walker, A. R., Suntzeff, N. B., et al. 1992, PASP, 104, 533

Hill, A. S., Benjamin, R. A., Kowal, G., et al. 2008, ApJ, 686, 363

Horne, K. 1986, PASP, 98, 609

Hynes, R. I. 2002, A&A, 382, 752

Inoue, S. 2004, MNRAS, 348, 999

Ioka, K. 2003, ApJL, 598, L79

Johnston, S., Keane, E. F., Bhandari, S., et al. 2017, MNRAS, 465, 2143

Katz, J. I. 2016, Modern Physics Letters A, 31, 1630013

Kauffmann, G., Heckman, T. M., Tremonti, C., et al. 2003, MNRAS, 346, 1055

Keane, E. F., Stappers, B. W., Kramer, M., & Lyne, A. G. 2012, MNRAS, 425, L71

Keane, E. F., Johnston, S., Bhandari, S., et al. 2016, Nature, 530, 453

Kennicutt, Jr., R. C., Tamblyn, P., & Congdon, C. E. 1994, ApJ, 435, 22

Kewley, L. J., & Dopita, M. A. 2002, ApJS, 142, 35

Kewley, L. J., Dopita, M. A., Sutherland, R. S., Heisler, C. A., & Trevena, J. 2001, ApJ, 556, 121

Kewley, L. J., & Ellison, S. L. 2008, ApJ, 681, 1183

Kewley, L. J., Geller, M. J., Jansen, R. A., & Dopita, M. A. 2002, AJ, 124, 3135

Kewley, L. J., Groves, B., Kauffmann, G., & Heckman, T. 2006, MNRAS, 372, 961

Kobulnicky, H. A., & Kewley, L. J. 2004, ApJ, 617, 240

Lelli, F., Verheijen, M., & Fraternali, F. 2014, A&A, 566, A71

Leloudas, G., Schulze, S., Krühler, T., et al. 2015, MNRAS, 449, 917

Lorimer, D. R., Bailes, M., McLaughlin, M. A., Narkevic, D. J., & Crawford, F. 2007, Science, 318, 777

Manchester, R. N., Hobbs, G. B., Teoh, A., & Hobbs, M. 2005, AJ, 129, 1993

Marcote, B., Paragi, Z., Hessels, J. W. T., Keimpema, A., & van Langevelde, H. J. e. a. 2017, ApJ, 000, 000

Masui, K., Lin, H.-H., Sievers, J., et al. 2015, Nature, 528, 523

Mauch, T., & Sadler, E. M. 2007, MNRAS, 375, 931

McQuinn, M. 2014, ApJL, 780, L33

Mignard, F., Klioner, S., Lindegren, L., et al. 2016, ArXiv e-prints, arXiv:1609.07255

Moffat, A. F. J. 1969, A&A, 3, 455

Murase, K., Kashiyama, K., & Mészáros, P. 2016, MNRAS, 461, 1498

Newburgh, L. B., Bandura, K., Bucher, M. A., et al. 2016, in Proc. SPIE, Vol. 9906, Society of Photo-Optical Instrumentation Engineers (SPIE) Conference Series, 99065X

Olausen, S. A., & Kaspi, V. M. 2014, ApJS, 212, 6

Papastergis, E., Cattaneo, A., Huang, S., Giovanelli, R., & Haynes, M. P. 2012, ApJ, 759, 138

Pardo, K., Goulding, A. D., Greene, J. E., et al. 2016, ApJ, 831, 203

Park, S., Yang, J., Oonk, J. B. R., & Paragi, Z. 2016, ArXiv e-prints, arXiv:1611.05986

Peng, C. Y., Ho, L. C., Impey, C. D., & Rix, H.-W. 2002, AJ, 124, 266

—. 2010, AJ, 139, 2097

Perley, D. A., Levan, A. J., Tanvir, N. R., et al. 2013, ApJ, 778, 128

Perley, D. A., Quimby, R. M., Yan, L., et al. 2016, ApJ, 830, 13

Petroff, E., Bailes, M., Barr, E. D., et al. 2015, MNRAS, 447, 246

Pettini, M., & Pagel, B. E. J. 2004, MNRAS, 348, L59

Piro, A. L. 2016, ApJL, 824, L32

Planck Collaboration, Ade, P. A. R., Aghanim, N., et al. 2016, A&A, 594, A13

Ravi, V., Shannon, R. M., & Jameson, A. 2015, ApJL, 799, L5

Ravi, V., Shannon, R. M., Bailes, M., et al. 2016, ArXiv e-prints, arXiv:1611.05758

Reines, A. E., Greene, J. E., & Geha, M. 2013, ApJ, 775, 116

Reines, A. E., Plotkin, R. M., Russell, T. D., et al. 2014, ApJL, 787, L30

Reines, A. E., Sivakoff, G. R., Johnson, K. E., & Brogan, C. L. 2011, Nature, 470, 66

Reynolds, R. J. 1977, ApJ, 216, 433

Schlafly, E. F., & Finkbeiner, D. P. 2011, ApJ, 737, 103

Schlafly, E. F., Finkbeiner, D. P., Schlegel, D. J., et al. 2010, ApJ, 725, 1175

Schlegel, D. J., Finkbeiner, D. P., & Davis, M. 1998, ApJ, 500, 525

Scholz, P., Spitler, L. G., Hessels, J. W. T., et al. 2016, ApJ, 883, 177

Spitler, L. G., Cordes, J. M., Hessels, J. W. T., et al. 2014, ApJ, 790, 101

Spitler, L. G., Scholz, P., Hessels, J. W. T., et al. 2016, Nature, 531, 202

Thornton, D., Stappers, B., Bailes, M., et al. 2013, Science, 341, 53

Vergani, S. D., Salvaterra, R., Japelj, J., et al. 2015, A&A, 581, A102

Williams, P. K. G., & Berger, E. 2016, ApJL, 821, L22